Research Article Vol. 34, No. 2 / 26 Jan 2026 / Optics Express 1465
Optics EXPRESS

High-performance PGC algorithm for a Φ-OTDR system based on multi-carrier mixing

TENG MA,[1,2] XUPING ZHANG,[1,2] BANGWEI LIU,[1,2] NASHEETA MAZHAR,[1,2] NINGMU ZOU,[1,3] YUANYUAN SHAN,[4,5] AND YIXIN ZHANG[1,2,6]

[1]College of Engineering and Applied Sciences, Nanjing University, Nanjing 210023, China
[2]Key Laboratory of Intelligent Optical Sensing and Manipulation, Ministry of Education, Nanjing University, Nanjing 210093, China
[3]School of Integrated Circuits, Nanjing University, Suzhou 215163, China
[4]School of Physics and Optoelectronic Engineering, Nanjing University of Information Science & Technology, Jiangsu, Nanjing, 210044, China
[5]violetsyy@nuist.edu.cn
[6]zyixin@nju.edu.cn

Abstract: The conventional phase-generated carrier (PGC) demodulation algorithm is often susceptible to three major disturbances in practical distributed fiber sensing applications, namely modulation depth, carrier phase delay, and laser intensity disturbance. These disturbances significantly render the Φ-OTDR system less capable of achieving high-accuracy vibration sensing under complex environmental conditions. To address these limitations, this study proposes a high-performance PGC demodulation algorithm based on multi-carrier mixing (PGC-MCM). By establishing mathematical logic operations between multiple mixed carrier signals and the intrinsic interference signal, the proposed method enables accurate reconstruction of the measured phase signal while effectively suppressing the influence of the aforementioned disturbances. Experimental results verify that the algorithm can precisely demodulate vibration signals with varying frequencies and amplitudes at different locations along the sensing fiber, achieving high fidelity recovery of the original signal. The proposed approach demonstrates excellent linearity and noise immunity. It yields a total harmonic distortion (THD) of −66.32 dB, a signal-to-noise and distortion ratio (SINAD) of 54.74 dB, with an amplitude error rate (R_{error}). as low as 0.46%, highlighting its strong potential for high-accuracy distributed optical fiber sensing applications.

1. Introduction

The phase-sensitive optical time-domain reflectometer (Φ-OTDR) enables precise monitoring of external vibration events by detecting phase variations in the Rayleigh backscattered light (RBS) within the sensing fiber [1–3]. Owing to its high sensitivity and fully distributed capability, Φ-OTDR has been widely applied in diverse fields including oil and gas pipeline protection [4,5], perimeter security [6,7], and railway condition monitoring [8,9].

At present, several phase demodulation algorithms—such as quadrature (I/Q) demodulation [10,11], 3 × 3 coupler demodulation [12–14], and PGC demodulation [15,16]—have been widely applied in Φ-OTDR system. Among these techniques, the PGC demodulation method has become one of the preferred approaches for phase retrieval due to its high sensitivity, wide dynamic range, and excellent linearity [17]. However, in practical implementations, the conventional PGC algorithm is limited by various non-ideal disturbances [18,19]. The three most significant disturbances are modulation depth (MD), carrier phase delay (CPD), and light intensity disturbance (LID). Specifically, deviation in MD is mainly caused by variations in the carrier signal amplitude and environmental temperature characteristics [20]; CPD arises from the

#584056 https://doi.org/10.1364/OE.584056
Journal © 2026 Received 7 Nov 2025; revised 11 Dec 2025; accepted 25 Dec 2025; published 12 Jan 2026

Optics EXPRESS

time delay between the carrier signal and the interference signal [21]; and LID is induced by optical source instability or environmental perturbations [22].

To mitigate the adverse effects of these three disturbances on demodulation accuracy, numerous improved PGC algorithms have been proposed. Tong et al. proposed an improved PGC Differential cross multiplication (PGC-DCM) algorithm by introducing a correction in the differential cross-multiplication step [23], effectively suppressing nonlinear errors caused by optical-intensity disturbances. Li et al. developed PGC-SCR, which achieves real-time carrier phase compensation through synchronous carrier recovery, significantly reducing THD [24]. Building on this, Zhang and Li introduced PGC-AD-DSM, which combines asymmetric division with differential self-multiplication [25], not only mitigating errors caused by modulation depth drift but also further enhancing robustness against optical-intensity fluctuations. Sun et al. proposed a differential self-division method based on PGC Arctangent (PGC-Arctan) algorithm [26], effectively suppressing modulation depth effects and demonstrating good stability and noise resilience. Subsequently, Xiao et al. presented an improved PGC algorithm applied to Φ-OTDR system [27], which effectively suppresses both linear and nonlinear distortions induced by modulation depth variations and carrier phase delay. Although the aforementioned studies have demonstrated that introducing multiple carrier-mixing paths can achieve signal demodulation while mitigating certain disturbances, few approaches are capable of simultaneously eliminating all three types of interference. Moreover, most of these works did not clearly explain the rationale behind the selection of specific carrier-mixing signals.

In this paper, we analyze the multi-order carrier mixing scheme and provide a theoretical guideline for selecting the appropriate mixing orders. Based on this analysis, the optimal carrier harmonics to be introduced are identified, and an improved demodulation algorithm is proposed. The aim is to achieve accurate phase recovery while simultaneously suppressing the effects of MD, CPD, and LID. This approach will significantly enhance system robustness and improve signal reconstruction accuracy.

2. Principle

2.1. Φ-OTDR system employing a PGC scheme

The basic principle of Φ-OTDR is to detect the phase variations of coherent RBS induced by numerous scattering centers within the duration of the injected optical pulse [28]. When a PGC based unbalanced Michelson interferometer (MI) is introduced at the receiver, the RBS signal from a vibration point along the sensing fiber is directed into the MI through a circulator and interferes with the local carrier signal, thereby generating an interference signal whose phase carries the sensing information. The phase of this interference swignal varies with the external disturbances, and can be demodulated with high sensitivity through the PGC modulation and demodulation process. The system configuration of the Φ-OTDR with PGC detection is illustrated in Fig. 1.

Assuming that the sensing fiber is composed of continuous scattering units with a length of ΔL [29], each scattering unit contains i randomly distributed scattering centers whose polarization states are identical. The backscattered optical field at a distance $L_i = \Delta L$ can be expressed as:

$$E_{L_i}(t) = E_0 P_i \exp(-\alpha L_i) \exp(-i2\beta L_i) a_i \exp[j\varphi_i(t)] \tag{1}$$

where E_0 is the electric field amplitude of the incident light, P_i denotes the polarization-related coefficient, α represents the optical power attenuation coefficient, β is the propagation constant, and a_i and φ_i are the reflectivity and phase of the scattering unit, respectively.

As shown in Fig. 1, the light source is a narrow-linewidth laser whose coherence length is longer than the pulse width, ensuring that the Rayleigh backscattered lights overlapped within one spatial resolution length can interfere with each other. When the optical field $E_l(t)$ enters

Optics EXPRESS

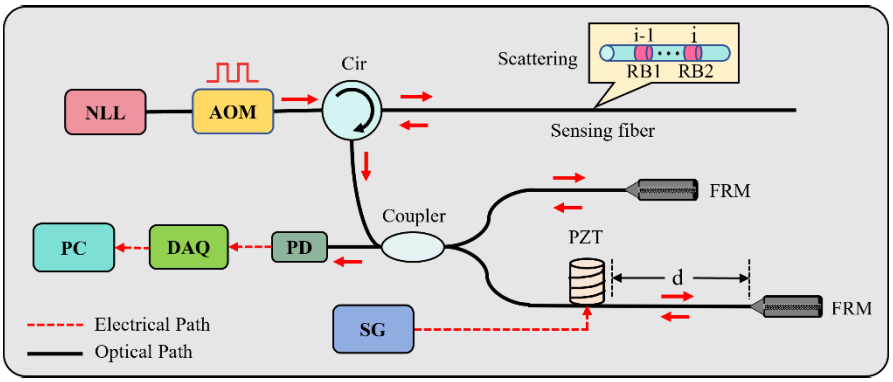

Fig. 1. Schematic diagram of Φ-OTDR system based on PGC detection

the unbalanced MI structure, the backscattered components RB_1 and RB_2 interfere due to their identical optical path lengths. One arm of the MI serves as a delay path with an optical path difference of d; therefore, the interference electric field $E(t)$ at a distance L can be expressed as:

$$\begin{aligned} E(t) &= E_L(t) + E_{L-d}(t) \\ &= E_0 P_L \exp(-\alpha L) \cdot \exp(-j2\beta L) \cdot a_L \exp[j\varphi_L(t)] \\ &\quad + E_0 P_{L-d} \exp[-\alpha(L-d)] \cdot \exp[-j2\beta(L-d)] \\ &\cdot a_{L-d} \exp[j\varphi_L(t)] \cdot \exp[j\varphi_{L-d}(t) - j\varphi_L(t)] \\ &= M + Nexp[j\beta d + \Delta\varphi(t)] \end{aligned} \tag{2}$$

Assuming that $\Delta\varphi(t) = \varphi_{L-d}(t) - \varphi_L(t)$, and simplifying the coefficients M and N, the output optical power of the interference through the MI can be expressed as:

$$I(t) = |E(t)|^2 = M^2 + N^2 + 2MN\cos[\beta d + \Delta\varphi(t)] = A + B\cos\varphi(t). \tag{3}$$

A sinusoidal signal with a modulation angular frequency of ω_c is applied to the other arm of the MI, introducing an additional phase modulation $C\cos(\omega_c t)$ in Eq. (3). Accordingly, the interference intensity can be rewritten as:

$$I(t) = A + B\cos[C\cos(\omega_c t) + \varphi(t)] \tag{4}$$

where A is the direct current (DC) component, B is the alternating current (AC) component, C denotes the modulation depth, ω_c represents the carrier frequency, and $\varphi(t)$ corresponds to the measurand signal.

2.2. Basic principle of the traditional PGC demodulation algorithm

In practical conditions, both the LID and the CPD (θ) affect the interference signal. Therefore, by introducing these nonideal disturbances into Eq. (4), the interference signal detected by the photodetector can be expressed as:

$$I(t) = (1 + m\cos\omega_n t)\{A + B\cos[C\cos(\omega_c t + \theta) + \varphi(t)]\} \tag{5}$$

where m is the amplitude of the optical intensity disturbance, and ω_n is its angular frequency.

Optics EXPRESS

Based on the Bessel function relationship, Eq. (5) can be expanded as follows:

$$I(t) = (1 + m\cos\omega_n t)\left\{\begin{array}{l} A + B\cos[\varphi(t)]\left[J_0(C) + 2\sum\limits_{k=1}^{\infty}(-1)^k J_{2k}(C)\cos(2k(\omega_c t + \theta))\right] \\ -B\sin[\varphi(t)]\left[2\sum\limits_{k=0}^{\infty}(-1)^k J_{2k+1}(C)\cos((2k+1)(\omega_c t + \theta))\right] \end{array}\right\} \quad (6)$$

where $J_0(C)$ denotes the zero-order Bessel function, while $J_{2k}(C)$ and $J_{2k+1}(C)$ represent the even-order and odd-order Bessel functions, respectively.

At this point, the interference signal is multiplied by the fundamental frequency of the carrier signal $\cos(\omega_c t)$ and second harmonic $\cos(2\omega_c t)$, respectively, and then passed through a low-pass filter, yielding the in-phase and quadrature components as follows:

$$I_{1s} = LPF[I(t)\cdot\cos(\omega_c t)] = -(1 + m\cos\omega_n t)BJ_1(C)\cos\theta\sin\varphi(t) \quad (7)$$

$$I_{2s} = LPF[I(t)\cdot\cos(2\omega_c t)] = -(1 + m\cos\omega_n t)BJ_2(C)\cos 2\theta\cos\varphi(t) \quad (8)$$

In the PGC-DCM algorithm, the two obtained signals are first differentiated and then cross-multiplied; performing a subsequent differential operation yields I_D:

$$I_D = (1 + m\cos\omega_n t)^2 B^2 J_1(C)J_2(C)cos\theta cos2\theta\varphi'(t) \quad (9)$$

By integrating I_D, the phase $\varphi(t)$ can be obtained. It can be seen that the PGC-DCM algorithm is influenced by the MD, CPD, and LID. The variation of the coefficient term $(1 + m\cos\omega_n t)^2 B^2 J_1(C)J_2(C)cos\theta cos2\theta$ in I_D with respect to C is shown in Fig. 2(a). The overall absolute magnitude of the coefficient term of I_D remains much smaller than 1. However, when the modulation depth $C = 2.37$ rad, the magnitude reaches its maximum. Under this condition, the demodulation performance of the DCM algorithm is optimal, indicating that $C = 2.37$ rad is the best operating point for DCM-based demodulation. Figure 2(b) illustrates the disturbances of CPD and LID on the coefficient term of I_D when $C = 2.37$ rad. It is evident that the PGC-DCM algorithm achieves its best demodulation performance only under ideal conditions. When CPD and LID deviate from the ideal case (i.e., LID$\neq$ 1 rad, $\theta \neq k\pi$ rad, $k \in Z$), the magnitude of the coefficient term in I_D decreases further.

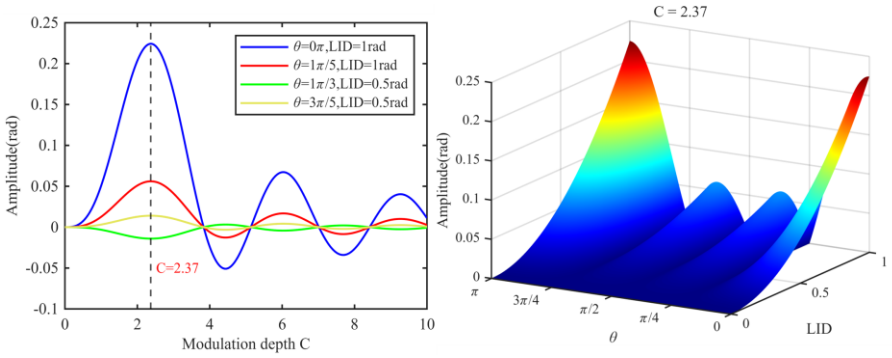

Fig. 2. The influence of non-ideal disturbances on the PGC-DCM

In the PGC-Arctan algorithm, the two extracted signals are divided, and the resulting signal can be expressed as I_A:

$$I_A = \frac{J_1(C)\cos\theta}{J_2(C)\cos 2\theta}\tan\varphi(t) \quad (10)$$

By applying the arctangent operation to I_A, the phase $\varphi(t)$ can be obtained. It can be seen that the PGC-Arctan algorithm is affected by both the MD and the CPD. Figure 3(a) shows that

Optics EXPRESS

only for specific values, such as $C = 2.63$ rad, can the PGC-Arctan algorithm eliminate the influence of MD. The variation of the coefficient term $J_1(C)\cos\theta/J_2(C)\cos 2\theta$ in I_A with respect to C is illustrated in Fig. 3(b). As shown in Fig. 3(b), changes in CPD alter the effective MD, making it more difficult for the absolute magnitude of the coefficient term of I_A to remain near 1. This further limits the ability of the PGC-Arctan algorithm to achieve ideal demodulation performance.

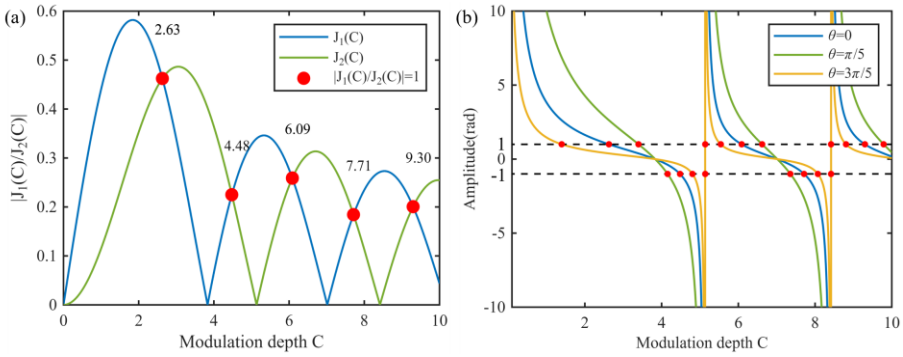

Fig. 3. The influence of non-ideal disturbances on the PGC-Arctan.

2.3. *Disturbances suppression via multi-order carrier mixing*

First, the basic principle of the multi-carrier mixing method is that, during demodulation of the interference signal detected by the photodetector, the signal is mixed with the k-th harmonic of the carrier and then low-pass filtered to extract the k-th order component. This process retains the baseband term that is related to $\varphi(t)$. Therefore, the coefficients in the expression of the signal obtained after the k-th mixing and low-pass filtering primarily originate from the Bessel function term $J_k(C)$.

Considering that $\varphi(t)$ is much smaller compared with the carrier signal, the result obtained after mixing the interference signal with the k-th harmonic of the carrier $cos(k\omega_c t)$, followed by low-pass filtering, can be approximated as:

$$S_k(t) \approx B \cdot J_k(C) \cdot \Gamma_k(\theta) \cdot \varphi(t) + m \cdot B \cdot J_k(C) \cdot \Delta_k(\theta, \omega_n, t) + n_k(t) \tag{11}$$

where Γ_k and Δ_k are constant coefficients determined by the CPD θ, and $n_k(t)$ denotes the projection of measurement noise onto this channel, including optical noise, electronic noise, etc. In the above expression, the first term contains the information to be measured, i.e., the useful signal component, whose amplitude is proportional to $J_k(C)$. The second term is the cross-interference component produced by the interaction between optical-intensity disturbance and the carrier, which may be projected onto the baseband after mixing or filtering.

Since the amplitude of the information term is proportional to $J_k(C)$, the signal energy in the k-th channel is approximately $\propto J_k(C)^2$. Assuming that the noise power in different channels remains approximately equal, the Carrier to Noise Ratio (CNR) of the k-th channel can be expressed as:

$$CNR_k \propto \frac{(B \cdot J_k(C) \cdot \Gamma_k(\theta))^2}{\sigma_n^2} \propto J_k(C)^2 \tag{12}$$

where B, Γ_k, and σ_n^2 can be regarded as constants that show no strong dependence on k.

Optics EXPRESS

For a fixed modulation depth C, the variation of the Bessel function term $J_k(C)$ with respect to k can be approximated as:

$$J_k(C) \approx \frac{(C/2)^k}{k!} \tag{13}$$

It can be seen that $J_k(C)$ decays rapidly with increasing k (factorial-level decay). Therefore, as the carrier harmonic order k increases, the signal energy of the information term in a single channel exhibits factorial attenuation, causing the corresponding CNR_k to drop rapidly and become unusable, which severely degrades demodulation performance.

The approximate expression for each channel described in Eq. (11) can be linearly represented as:

$$S_k(t) = a_k \cdot \varphi(t) + b_k \cdot m + c_k \cdot \delta\theta + d_k \cdot \delta C + n_k(t) \tag{14}$$

here, the coefficient $a_k \propto J_k(C)$, while b_k, c_k, $d_k$is related to $J_k(C)$ and θ, and also decays rapidly as k increases.

Assuming that the first k mixing channels S_1,. . . , S_k are used simultaneously to solve for certain parameters in $x = [\varphi(t), m, \theta, C]^T$ while eliminating the influence of other parameters, the above expression can be rewritten in matrix form as:

$$\mathbf{S}(t) = \mathbf{H}\mathbf{x}(t) + \mathbf{n}(t), \qquad \mathbf{H} = \begin{bmatrix} a_1 & b_1 & c_1 & d_1 \\ a_2 & b_2 & c_2 & d_2 \\ \vdots & \vdots & \vdots & \vdots \\ a_k & b_k & c_k & d_k \end{bmatrix}, \qquad \mathbf{x} = \begin{bmatrix} \varphi \\ m \\ \delta\theta \\ \delta C \end{bmatrix} \tag{15}$$

where H is a $k \times p$ coefficient matrix, and p is the number of unknowns, which equals 4. To estimate $\varphi(t)$ while suppressing the remaining terms using least squares or a pseudo-inverse, the solution is generally expressed as:

$$\hat{\mathbf{X}} = (\mathbf{H}^\mathbf{T}\mathbf{H})^{-1}\mathbf{H}^\mathbf{T}\mathbf{S} \tag{16}$$

The noise amplification is determined by the norm of $(\mathbf{H}^\mathbf{T}\mathbf{H})^{-1}$. Because the first column of $\mathbf{H}$ is distributed on the order of $J_k(C)$, the column scaling becomes inconsistent (large for low-order terms and extremely small for high-order terms). As a result, the condition number of $\mathbf{H}$ increases significantly, and $(\mathbf{H}^\mathbf{T}\mathbf{H})^{-1}$ greatly amplifies noise and estimation errors, leading to substantial estimation errors in $\hat{\varphi}$.

In addition, we investigate the lower bound on introducing multiple harmonic carriers. For the interference signal expression described in Eq. (5), several terms can be redefined as follows:

$$U(t) = (1 + m\cos\omega_n t) \tag{17}$$

$$\Phi(t) = \omega_c t + \theta \tag{18}$$

Applying the Jacobi–Anger expansion to the cosine term in Eq. (5) (retaining only the dominant 0th-, 1st-, and 2nd-order terms) yields:

$$\begin{aligned} cos(Ccos\Phi(t) + \varphi(t)) = J_0(C)cos\varphi(t) - 2J_1(C)sin\varphi(t)cos\Phi(t) \\ - 2J_2(C)cos\varphi(t)cos2\Phi(t) + \cdots \end{aligned} \tag{19}$$

Substituting the above expression into Eq. (5), then mixing the interference signal with the fundamental cosine carrier, the fundamental sine carrier, the second-harmonic cosine carrier, and the second-harmonic sine carrier, followed by low-pass filtering, we obtain:

Optics EXPRESS

First-order baseband components:

$$L_1 = LPF\{I(t)\cos(\omega_c t)\} = M(t)B(-J_1(C)\sin\varphi(t))\cos\theta \tag{20}$$

$$Q_1 = LPF\{I(t)\sin(\omega_c t)\} = M(t)B(-J_1(C)\sin\varphi(t))\sin\theta \tag{21}$$

Second-order baseband components:

$$I_2 = LPF\{I(t)\cos(2\omega_c t)\} = M(t)B(-J_2(C)\cos\varphi(t))\cos 2\theta \tag{22}$$

$$Q_2 = LPF\{I(t)\sin(2\omega_c t)\} = M(t)B(-J_2(C)\cos\varphi(t))\sin 2\theta \tag{23}$$

Furthermore, to generalize the above analysis to arbitrary harmonic order, we start again from Eq. (5), and omitting the DC component, we let $J_k(\cdot)$denote the k-th-order Bessel function. When the interference signal is mixed with the k-th harmonic of the carrier and its corresponding sine term, and then passed through a low-pass filter, the baseband in-phase and quadrature components can be written in the unified form

$$I_k(t) = LPF\{I(t)\cos(k\omega_c t)\} = -M(t)BJ_k(C)\Gamma_k(\varphi(t))\cos(k\theta) \tag{24}$$

$$Q_k(t) = LPF\{I(t)\sin(k\omega_c t)\} = -M(t)BJ_k(C)\Gamma_k(\varphi(t))\sin(k\theta) \tag{25}$$

where $\Gamma_k(\varphi(t))$is a phase function determined by the parity of k: $\Gamma_k(\varphi(t)) = \sin[\varphi(t)]$. when $k$is odd, and $\Gamma_k(\varphi(t)) = \cos[\varphi(t)]$ when k is even. Thus, for any k, the magnitude of the baseband vector is given by

$$R_k(t) = \sqrt{I_k^2(t) + Q_k^2(t)} = M(t)B|J_k(C)||\Gamma_k(\varphi(t))| \tag{26}$$

Now consider sampling the same spatial position at N discrete time instants $t_i (i = 1, \ldots, N)$. Suppose that only two harmonic orders $k = p$ and $k = q$ are used (for example $p = 1,\ \ q = 2$ or $p = 1,\ \ q = 3$). At each instant, the observable sideband magnitudes consist of the two sequences $R_p(t_i)$ and $R_q(t_i)$, yielding $2N$ scalar samples. In addition, the I–Q phase relationship, i.e., the direction of the vector $\{I_k(t), Q_k(t)\}$, can provide at most one global angular constraint on the carrier phase delay θ. Hence, the total number of independent observables is $N_{obs} = 2N + 1$. By contrast, the true unknowns of the system include the instantaneous quantities $M(t_i)$ and $\varphi(t_i)$ at each time instant (a total of $2N$ degrees of freedom), as well as the two global variables $C$and θ, so that $N_{unk} = 2N + 2$. Clearly, $N_{\text{obs}} - N_{\text{unk}} = -1$, which means that the system is underdetermined and a unique solution cannot be obtained.

A special case arises when both $p$and $q$are odd (for example $p = 1,\ \ q = 3$). In this case, $\Gamma_p[\varphi(t)] = \Gamma_q[\varphi(t)] = \sin[\varphi(t)]$, and therefore the two magnitude sequences satisfy

$$\frac{R_q(t)}{R_p(t)} = \frac{J_q(C)}{J_p(C)} \tag{27}$$

In other words, the second sequence does not provide any new time-varying information; it only supplies a constant ratio determined by C. Algebraically, the observation equations can constrain only the overall scale of $M(t)\sin[\varphi(t)]$ and this constant ratio. Thus, the three quantities $M(t)$, $\varphi(t)$, and Ccannot be uniquely separated using only these two equations.

Only when the harmonic orders $p$and $q$have different parity (for example $p = 1,\ \ q = 2$) do the two magnitude sequences respectively contain $\sin[\varphi(t)]$ and $\cos[\varphi(t)]$, thereby forming an orthogonal basis with respect to $\varphi(t)$. In this case, after eliminating the global constant term (or cancelling $M(t)$ by taking an appropriate ratio), there remains a residual coupling associated with the modulation depth C. Consequently, a third independent observation or suitable prior information is still required to completely remove the dependence on C.

In summary, we conclude that to eliminate the influence of the three typical disturbances (MD, CPD, and LID) while achieving accurate signal demodulation, introducing third-harmonic carrier mixing is the critical and optimal choice.

Optics EXPRESS

2.4. Theory of the PGC-MCM algorithm

Based on the above theory, this work proposes a PGC-MCM algorithm with third-harmonic carrier mixing. Figure 4 illustrates the principle of the PGC-MCM algorithm.

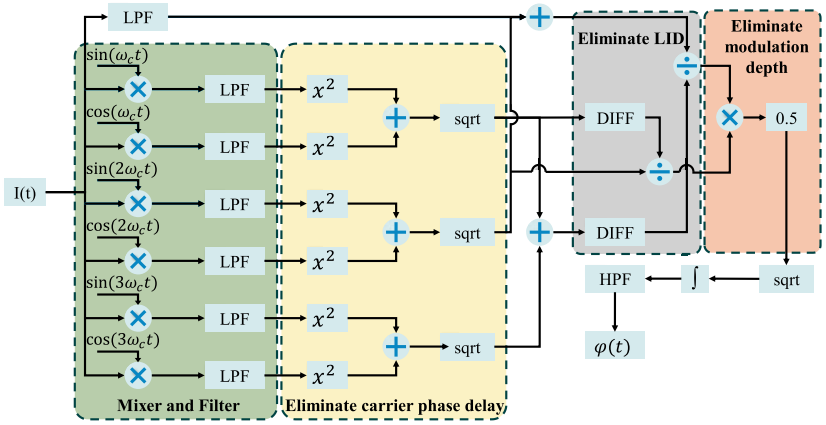

Fig. 4. PGC-MCM demodulation algorithm schematic diagram

The interference signal $I(t)$ is multiplied by $\cos(\omega_c t)$, $\sin(\omega_c t)$, $\cos(2\omega_c t)$, $\sin(2\omega_c t)$, $\cos(3\omega_c t)$, $\sin(3\omega_c t)$ to obtain six mixed signals, which are then passed through low-pass filters to remove higher-order harmonic components, yielding $L_0(t)$ through $L_6(t)$.

$$\begin{cases} L_0(t) = LPF[I(t)] = (1 + m\cos\omega_n t)BJ_0(C)\cos\varphi(t) \\ L_1(t) = LPF[I(t)\sin\omega_c t] = -(1 + m\cos\omega_n t)BJ_1(C)\sin\theta\sin\varphi(t) \\ L_2(t) = LPF[I(t)\cos\omega_c t] = -(1 + m\cos\omega_n t)BJ_1(C)\cos\theta\sin\varphi(t) \\ L_3(t) = LPF[I(t)\sin 2\omega_c t] = -(1 + m\cos\omega_n t)BJ_2(C)\sin 2\theta\cos\varphi(t) \\ L_4(t) = LPF[I(t)\cos 2\omega_c t] = -(1 + m\cos\omega_n t)BJ_2(C)\cos 2\theta\cos\varphi(t) \\ L_5(t) = LPF[I(t)\sin 3\omega_c t] = -(1 + m\cos\omega_n t)BJ_3(C)\sin 3\theta\sin\varphi(t) \\ L_6(t) = LPF[I(t)\cos 3\omega_c t] = -(1 + m\cos\omega_n t)BJ_3(C)\cos 3\theta\sin\varphi(t) \end{cases} \tag{28}$$

Next, exploiting the orthogonal phase properties of sine and cosine, $L_1(t)$ and $L_2(t)$ are squared, summed, and square-rooted to eliminate the carrier phase delay, producing $P_1(t)$. The same procedure is applied to $L_3(t)$ and $L_4(t)$, as well as $L_5(t)$ and $L_6(t)$, yielding $P_2(t)$ and $P_3(t)$, respectively.

$$\begin{cases} P_1(t) = \sqrt{L_1^2(t) + L_2^2(t)} = (1 + m\cos\omega_n t)BJ_1(C)\sin\varphi(t) \\ P_2(t) = \sqrt{L_3^2(t) + L_4^2(t)} = (1 + m\cos\omega_n t)BJ_2(C)\cos\varphi(t) \\ P_3(t) = \sqrt{L_5^2(t) + L_6^2(t)} = (1 + m\cos\omega_n t)BJ_3(C)\sin\varphi(t) \end{cases} \tag{29}$$

Summing $P_1(t)$ and $P_3(t)$ and differentiating with respect to time t gives $D_1(t)$. Summing $L_0(t)$ and $P_2(t)$ yields $D_2(t)$, and differentiating $P_1(t)$ with respect to t produces $D_3(t)$.

$$D_1(t) = \frac{d[P_1(t) + P_3(t)]}{dt} = (1 + m\cos\omega_n t)B[J_1(C) + J_3(C)]\cos\varphi(t)\varphi'(t) \tag{30}$$

$$D_2(t) = L_0(t) + P_2(t) = (1 + m\cos\omega_n t)B[J_0(C) + J_2(C)]\cos\varphi(t) \tag{31}$$

Optics EXPRESS

$$D_3(t) = \frac{d[P_1(t)]}{dt} = (1 + m\cos\omega_n t)BJ_1(C)\cos\varphi(t)\varphi'(t) \tag{32}$$

Using the recurrence properties of Bessel functions:

$$J_{k-1}(C) + J_{k+1}(C) = \frac{2kJ_k(C)}{C} \tag{33}$$

Equations (30) and (31) can be transformed as follows:

$$R_1(t) = \frac{4BJ_2(C)\cos\varphi(t)\varphi'(t)(1 + m\cos\omega_n t)}{C} \tag{34}$$

$$R_2(t) = \frac{2BJ_1(C)\cos\varphi(t)(1 + m\cos\omega_n t)}{C} \tag{35}$$

Dividing $R_1(t)$ by $R_2(t)$ gives:

$$Q_1(t) = 2\frac{J_2(C)}{J_1(C)}\varphi'(t) \tag{36}$$

Dividing $D_3(t)$ by $P_2(t)$ gives:

$$Q_2(t) = \frac{J_1(C)}{J_2(C)}\varphi'(t) \tag{37}$$

At this stage, $Q_1(t)$ and $Q_2(t)$ no longer contain the optical-intensity AC component B or the LID term, thereby eliminating the influence of LID on the demodulation results. Multiplying $Q_1(t)$ and $Q_2(t)$, and then dividing by 2 yields:

$$Z(t) = [\varphi'(t)]^2 \tag{38}$$

Finally, through square-rooting, integration, and high-pass filtering, the target phase signal $\varphi(t)$ can be obtained. In addition, to mitigate numerical instability caused by zero-valued samples during the computation, we incorporate a constant-bias compensation in the implementation, thereby further improving the robustness of the algorithm.

Based on this principle, the demodulated result of the improved algorithm contains only the target signal, and is no longer a function of the DC/AC components of the interference signal, MD, CPD, or LID. This effectively avoids demodulation distortion caused by the three aforementioned disturbances, achieving accurate and robust demodulation performance.

3. Simulation and comparison

To fully demonstrate the demodulation performance of the proposed algorithm, this section validates the PGC-MCM algorithm through simulations and compares it with conventional PGC algorithms. The basic simulation parameters are set as follows: the DC/AC amplitude of the interference signal is 1 rad; the modulation frequency of the carrier signal is 1 MHz; the vibration signal is a cosine wave with an amplitude of 10 rad and a frequency of 2 kHz; and the sampling rate is 16 Ms/s.

Simulations are performed using two typical modulation depths, 2.37 rad and 2.63 rad, two carrier phase delays, $\theta = 0$ and $\theta = 3\pi/5$, and two light-intensity disturbance frequencies, $\omega_n = 20$Hz and $\omega_n = 200$Hz. The combinations of MD, CPD, and LID in Fig. 5 are deliberately chosen to span from nearly ideal to strongly disturbed conditions, so that the performance differences among the algorithms can be clearly demonstrated. The resulting time-domain waveforms are shown in Fig. 5(a)-(f). Comparing Fig. 5(a)-(d), it can be seen that the PGC-Arctan and PGC-DCM algorithms exhibit varying degrees of amplitude distortion and waveform deformation when deviating from their respective optimal modulation depths. This distortion becomes more pronounced in the presence of carrier phase delay. In contrast, the proposed

Optics EXPRESS

PGC-MCM algorithm is unaffected by these two disturbances. Furthermore, combining Fig. 5(a), (e) and (f), it is evident that the PGC-DCM algorithm is significantly influenced by optical-intensity disturbance, resulting in severe waveform distortion in the time domain. In contrast, the PGC-MCM algorithm remains unaffected, providing stable and reliable demodulation that accurately restores the original signal.

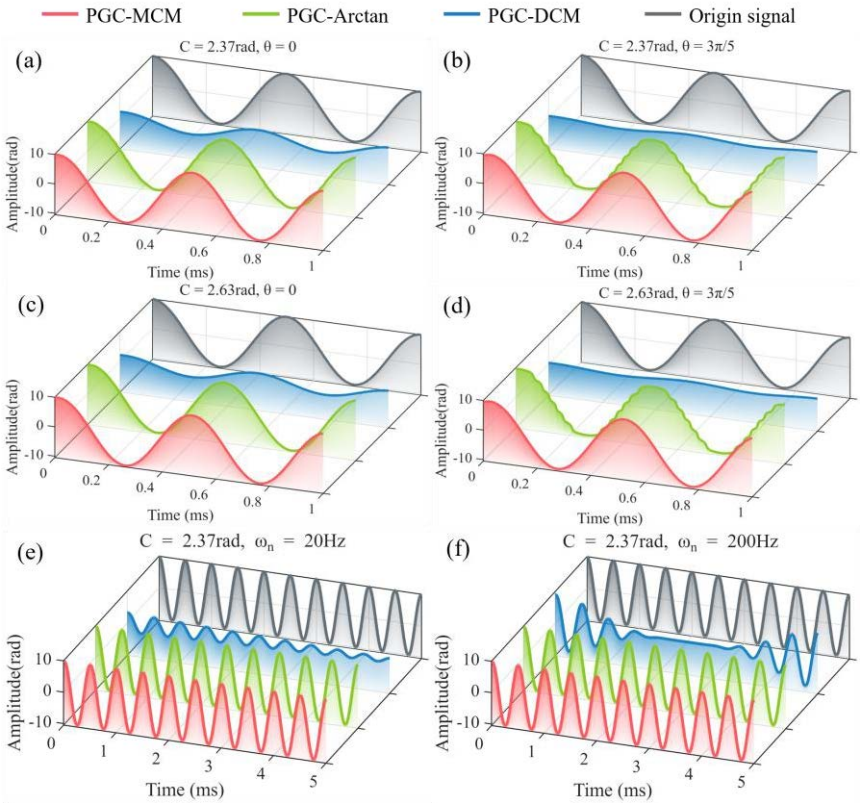

Fig. 5. Demodulation results under different modulation depths, carrier phase delays and light intensity disturbances.

Here, we present the power spectral density (PSD) plots corresponding to Fig. 5(a) and (d), as shown in Fig. 6. It can be seen that under non-ideal conditions, the PGC-Arctan algorithm generates a significant number of harmonics. The PGC-DCM algorithm exhibits an overall lower spectral amplitude, which corresponds to the amplitude distortion observed in the time-domain signals in Fig. 5. In contrast, the proposed PGC-MCM algorithm is largely unaffected by these non-ideal disturbances, maintaining a stable and consistent performance.

Further simulations were conducted considering that, in practical applications, the interferometric structure may be affected by environmental disturbances, making it difficult to maintain the modulation depth at its optimal value and potentially introducing carrier phase delay. In this study, the modulation depth C was varied from 1.0 rad to 3.5 rad in steps of 0.5 rad, the carrier phase delay is fixed at 0π, and LID is set to 0 dB. In addition, the CPD varies from 0 to 2π in steps of $\pi/5$, the modulation depth C is fixed at 2.63 rad, and LID is set to 0 dB. Finally, let $m = 1$, the LID frequency steps from 20 Hz to 200,000 Hz in a 10-fold variation, the modulation depth C is fixed at 2.63 rad, and the carrier phase delay is fixed at 0π. The demodulation performance was evaluated using total harmonic distortion (THD) and signal-to-noise and distortion ratio (SINAD). The resulting fitting results are shown in Fig. 7(a)–(f).

Optics EXPRESS

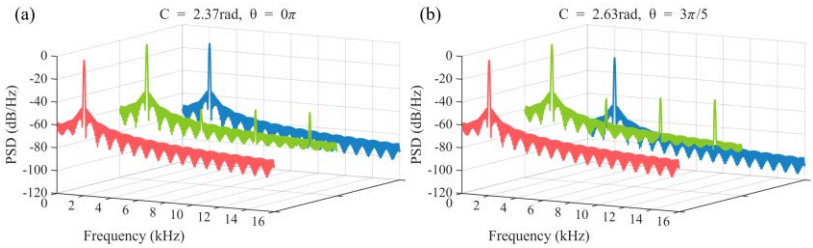

Fig. 6. PSD of different PGC algorithms

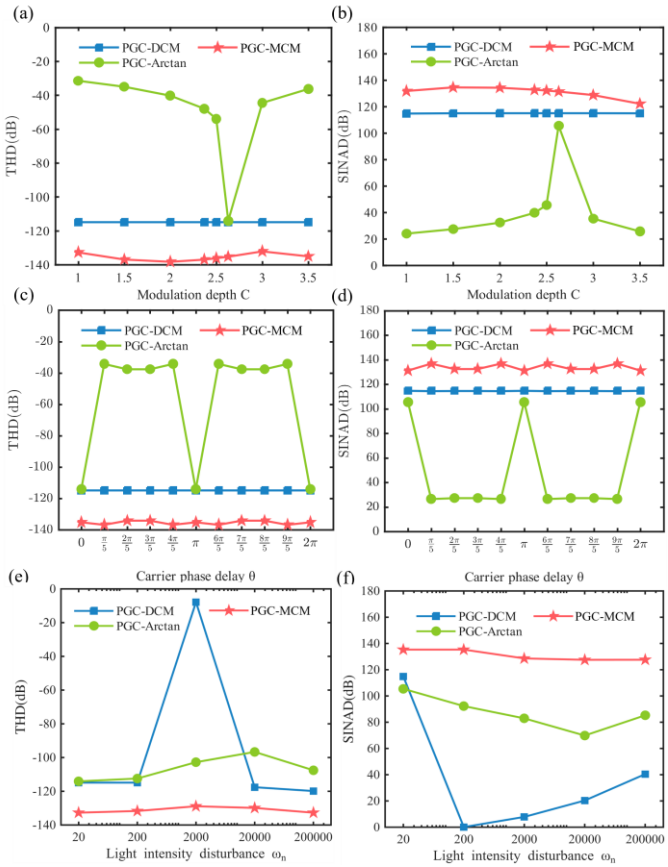

Fig. 7. THD/SINAD of demodulation results under different modulation depths and carrier phase delays. (a)(b) THD and SINAD of demodulation results at different modulation depths; (c)(d) THD and SINAD of demodulation results under different carrier phase delays; (e)(f) THD and SINAD of demodulation results under different light intensity disturbances.

Optics EXPRESS

THD quantifies the degree of distortion by comparing the energy of harmonic components in a signal to that of the fundamental frequency component, while SINAD evaluates the extent of interference and distortion by comparing the energy of the fundamental component to the total energy of noise and distortion components. As shown in Fig. 7, the demodulation performance of the PGC-Arctan algorithm depends on both the MD and the CPD. At $C \neq 2.63$rad and $\theta \neq 0$, the PGC-Arctan algorithm exhibits significant nonlinear distortion, with high THD and low SINAD, resulting in poor signal quality. Even at the optimal MD, CPD can cause notable nonlinear distortion, and the THD and SINAD achieve their best values only at 0, π, and 2π. Furthermore, under the condition of changing the LID, the demodulated signal exhibits a certain degree of nonlinear distortion.

In contrast, the PGC-DCM algorithm produces demodulated signals with coefficients less than 1, so the amplitude of its outputs is always lower than that of the original signal. When deviating from the optimal MD, the PGC-DCM algorithm exhibits linear distortion but maintains relatively low THD and high SINAD. Similarly, under varying carrier phase delays, the demodulated signals also show linear distortion while still retaining low THD and high SINAD. Furthermore, under the condition of changing the LID, the demodulated signal exhibits significant nonlinear distortion. The proposed PGC-MCM algorithm, however, shows no significant distortion in the time-domain waveform under variations in MD, CPD or LID, while maintaining low THD and high SINAD. Specifically, compared with the PGC-Arctan algorithm at the optimal MD, the THD of PGC-MCM algorithm is reduced by 21.1 dB, and its SINAD is improved by up to 20.5 dB relative to PGC-DCM algorithm under optimal MD. Moreover, the overall performance remains stable, with fluctuations within 5 dB, consistently maintaining a high level of demodulation quality.

4. Experiments and results

The PGC-MCM algorithm was further applied to a Φ-OTDR system to experimentally verify its performance advantages. The MI-based Φ-OTDR experimental setup is shown in Fig. 8. In the experiment, a narrow-linewidth laser (NLL) at 1550.12 nm was used as the light source. An acousto-optic modulator (AOM) generated optical pulses with widths of 90 ns at a repetition rate of 20 kHz. The generated pulses were amplified by an erbium-doped fiber amplifier (EDFA) and then injected into the sensing fiber through a circulator. The total length of the sensing fiber was 3070 m. Two piezoelectric transducers (PZT1 and PZT2), each consisting of coiled single-mode fiber, were placed at 1020 m and 2010 m along the fiber to serve as vibration sources, driven by a signal generator (SG). When a vibration occurs, the phase of the Rayleigh backscattered (RBS) light in the sensing fiber changes. This phase-modulated light is directed through the circulator into the MI structure, where it interferes with a high-frequency carrier signal at 1 MHz and 2 rad amplitudes at a 3 dB fiber coupler (50:50), producing an interference signal. The interference signal is detected by a high-sensitivity photodetector (PD) with a 70 MHz bandwidth. The PD output is sampled by an oscilloscope at 625 Ms/s and transferred to a computer. At specific locations along the fiber, the PGC-MCM algorithm, as illustrated in Fig. 4, is applied for subsequent digital demodulation on the computer.

In this system, the theoretical maximum detectable distance is given by $L<c/2fn_f$, which is set to 5 km. The spatial resolution is determined by $\Delta z = c \cdot \tau/2n_f$, and the calculation shows that, for a pulse width of $\tau = 90ns$, the corresponding theoretical spatial resolution is 9 m. To verify the spatial resolution of the system, a 2 kHz cosine signal was applied to drive PZT2. Figure 9 shows the vibration signal localization curve obtained after demodulation and smoothing. By comparing the 10% and 90% points of the rising edge [30], the actual system resolution is determined to be 9.2 m, which was in good agreement with the theoretical value.

To maintain system sensitivity, the optical path difference must be less than or equal to the theoretical spatial resolution associated with the pulse width [31]. Therefore, the unbalanced

Optics EXPRESS

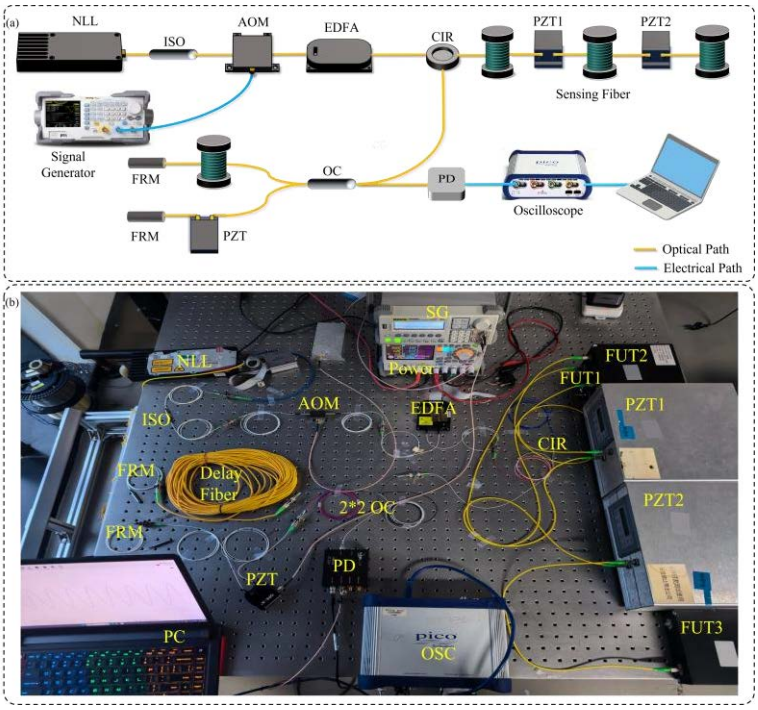

Fig. 8. Schematic of experimental setup.

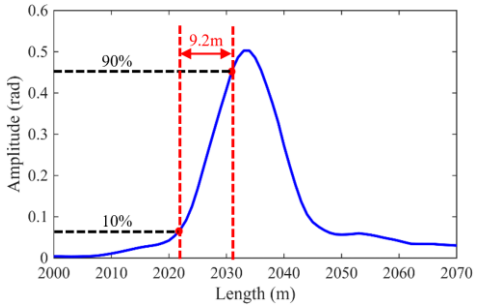

Fig. 9. Vibration event location curve.

Michelson interferometer in the system was configured with an optical path difference of 9 m. At PZT1, located at 1020 m, cosine vibration signals with a frequency of 1 kHz and amplitude of 1 rad, and a frequency of 1.5 kHz and amplitude of 2 rad, were applied. At PZT2, located at 2010 m, a continuous cosine vibration signal with a frequency of 2 kHz and amplitude of 2 rad was applied. Figure 10 presents the time–space and frequency–space diagrams of the globally demodulated signals at different locations in the PGC-based Φ-OTDR system. Comparing Fig. 10(a) and (b), it can be clearly seen that, under varying frequencies and amplitudes, the system is still able to accurately identify vibration events at different positions. Furthermore, comparing Fig. 10(c) and (d) shows that the demodulated signal frequencies match the applied vibration signals and the frequency–space information corresponds consistently with the time–space information.

Optics EXPRESS

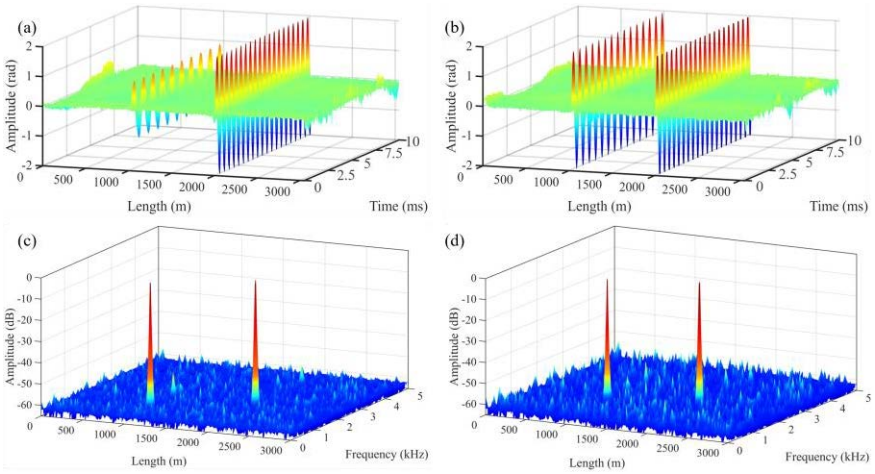

Fig. 10. The time-space diagrams and frequency-space diagrams of two vibration events. (a)(c) 1kHz, 1 rad signals and 2kHz, 2 rad signals at different positions; (b)(d) 1.5kHz, 2 rad signals and 2kHz, 2 rad signals at different positions.

To fully verify the superior performance of the proposed algorithm, it was compared with conventional PGC demodulation algorithms for the vibration signal at 2010 m. First, the demodulation performance of the PGC-DCM and PGC-Arctan algorithms at their respective optimal working points was validated (for the DCM algorithm, the modulation depth was 2.37 rad, CPD was 0 rad; for the Arctan algorithm, the modulation depth was 2.63 rad and CPD was 0 rad). The resulting demodulated signals are shown in Fig. 11(a)–(d). Subsequently, the proposed PGC-MCM algorithm was validated under a modulation depth of 2 rad and CPD was 0 rad, with the results shown in Fig. 11(g). To further compare the demodulation performance of the three algorithms under the influence of three typical disturbances and to validate the simulation results presented in Fig. 2 and Fig. 3, two sets of interference conditions were considered: a moderate interference scenario (modulation depth was 1.5 rad, CPD was $157\pi/180$) and a severe interference scenario (modulation depth was 3.5 rad, CPD was $87\pi/180$, with optical-intensity disturbance applied). The interference signals under these conditions were demodulated using all three algorithms. The resulting signals are shown in Fig. 11(b), (e), (h) for moderate interference and Fig. 11(c), (f), (i) for severe interference. Comparing the results in Fig. 11, it can be concluded that conventional PGC-DCM and PGC-Arctan algorithms exhibit varying degrees of amplitude and waveform distortion when subjected to the three typical disturbances, resulting in unstable demodulation performance. In contrast, the proposed PGC-MCM algorithm is unaffected by these typical disturbances, demonstrating excellent and stable demodulation performance.

Figure 12 shows the PSD of the conventional PGC-DCM and PGC-Arctan algorithms compared with the proposed PGC-MCM algorithm under the same parameter conditions corresponding to Fig. 11(a), (d) and (g). It can be seen that the proposed algorithm provides stronger harmonic suppression and better harmonic attenuation. Compared with the PGC-Arctan algorithm, the PGC-MCM algorithm exhibits lower harmonic components, lower noise levels and more concentrated energy in the demodulated signal. Compared with the PGC-DCM algorithm, the proposed algorithm shows higher main peaks and greater energy. As shown in Table 1, the PGC-MCM algorithm achieves a THD of -66.32 dB, a SINAD of 54.74 dB, and an amplitude error rate R_{error} of only 0.46% distortion. Compared with the PGC-Arctan algorithm, the THD is reduced by 33.10 dB, SINAD is increased by 21.83 dB, and R_{error} is reduced by 4.84%, indicating better signal restoration. Furthermore, compared with the PGC-DCM algorithm, the THD is reduced

Optics EXPRESS

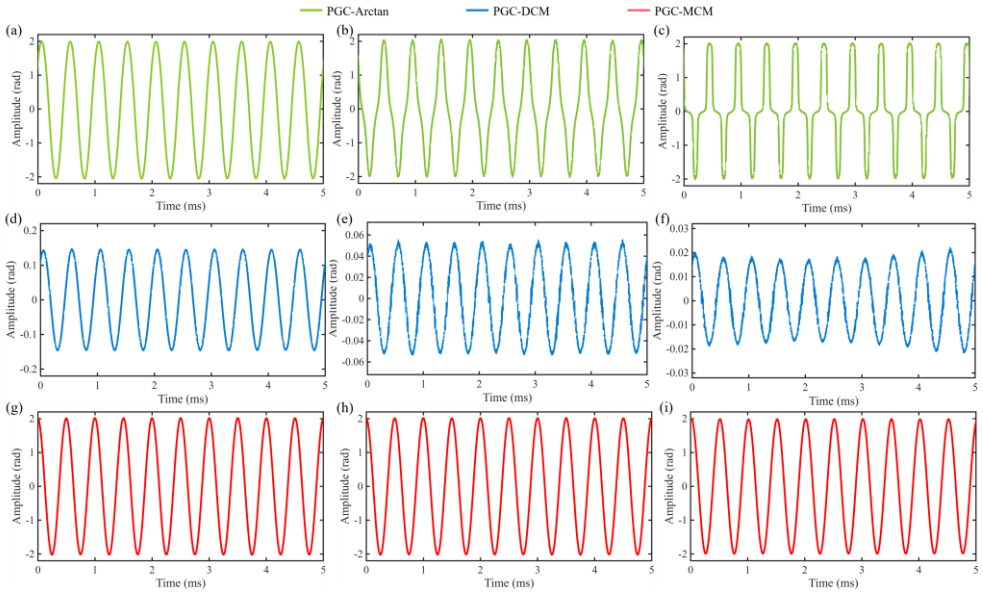

Fig. 11. Demodulation time domain results of different PGC algorithms.

by 10.66 dB, SINAD is increased by 28.67 dB, and R_{error} is reduced by 80.12%, representing a significant improvement. The high error of 80.58% observed in the PGC-DCM algorithm can be explained as follows: as shown in Fig. 2, the coefficient terms in the demodulated results of the PGC-DCM algorithm are inherently much smaller than 1 and the algorithm is highly sensitive to modulation depth and optical-intensity disturbances. As a result, the amplitude of its demodulated signal is much lower than 2 rad (as shown in Fig. 11(d)), leading to a very high error value.

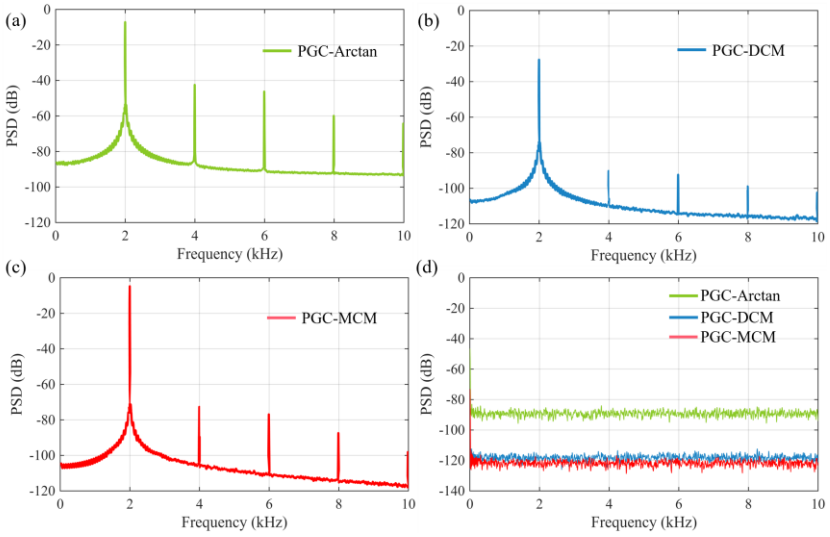

Fig. 12. PSD of different PGC algorithms.

Optics EXPRESS

Table 1. Performance of Different Demodulation Algorithms

Algorithm	THD (dB)	SINAD (dB)	R_{error} (%)
PGC-Arctan	-33.22	32.91	5.30
PGC-DCM	-55.66	26.07	80.58
PGC-MCM	-66.32	54.74	0.46

In addition, the noise-equivalent power (NEP) of the three algorithms was calculated. The NEP of the PGC-Arctan algorithm is $-44.59dBW/\sqrt{Hz}$, that of the PGC-DCM algorithm is $-59.02dBW/\sqrt{Hz}$, and the PGC-MCM algorithm also achieves $-60.85dBW/\sqrt{Hz}$. Therefore, the proposed method does not degrade the NEP performance. The PSD curves of the NEP for the three algorithms are shown in Fig. 12(d).

We further evaluate the feasibility of implementing the proposed algorithm in practical engineering systems. Although PGC-MCM employs six mixing channels and thus requires more operations than conventional single- or dual-channel schemes, its core computations (mixing, low-pass filtering, and basic arithmetic) are structurally regular and well suited to parallel and pipelined realization on DSPs, multi-core CPUs, GPUs, and FPGAs. The computational and hardware cost scales approximately linearly with the number of channels, so with current embedded processors and accelerator devices the proposed algorithm can be implemented in Φ-OTDR systems without compromising real-time demodulation performance.

5. Conclusion

In this work, we theoretically analyze how to select the appropriate mixing components in a multi-carrier mixing scheme, and on this basis, we propose an improved PGC algorithm (PGC-MCM). By introducing the fundamental, second-order, and third-order harmonics of the carrier for frequency mixing, the PGC-MCM effectively eliminates the nonlinear distortion induced by non-ideal factors such as MD, CPD, and LID. Both simulation and experimental results demonstrate that the algorithm maintains a low THD and high SINAD under the influence of all three disturbances, exhibiting excellent robustness and demodulation accuracy. Therefore, the proposed scheme provides a more reliable demodulation approach for Φ-OTDR system in high-sensitivity vibration monitoring and other engineering applications, showing significant potential for practical deployment.

Funding. National Natural Science Foundation of China (62175100); Fundamental Research Funds for the Central Universities (2024300447, 0213-14380264, 0213-14380265).

Disclosures. The authors declare no conflicts of interest.

Data availability. Data underlying the results presented in this paper are not publicly available at this time but may be obtained from the authors upon reasonable request.

References

1. Z. Sun, M. Fang, D. Huang, *et al.*, "An unsupervised learning method to enhance SNR for distributed optical fiber vibration sensor based on phase-sensitive OTDR," Opt. Laser Technol. **180**, 111570 (2025).
2. S. Li, Z. Qin, Z. Liu, *et al.*, "Long-distance OFDR with high spatial resolution based on time division multiplexing," J. Lightwave Technol. **41**(17), 5763–5772 (2023).
3. X. Zhang, Y. Zhang, L. Wang, *et al.*, "Current status and future of research and applications for distributed fiber optic sensing technology," Acta Opt. Sin. **44**(1), 0106001 (2024).
4. J. Zheng, Z. Sha, H. Feng, *et al.*, "Water hammer detection based on FIV online analysis using a distributed fiber optic sensor," Appl. Opt. **62**(28), 7455–7462 (2023).
5. F. Peng, H. Wu, X. Jia, *et al.*, "Ultra-long high-sensitivity Φ-OTDR for high spatial resolution intrusion detection of pipelines," Opt. Express **22**(11), 13804–13810 (2014).
6. P. Zhu, C. Xu, W. Ye, *et al.*, "Self-learning filtering method based on classification error in distributed fiber optic system," IEEE Sens. J. **19**(19), 8929–8933 (2019).
7. A. E. Alekseev, B. G. Gorshkov, D. A. Il'inskii, *et al.*, "A low-noise fiber phase-sensitive optical time-domain reflectometer for seismology application," Instrum. Exp. Tech. **66**(5), 837–842 (2023).

Optics EXPRESS

8. M. A. Rahman, H. Taheri, F. Dababneh, *et al.*, "A review of distributed acoustic sensing applications for railroad condition monitoring," Mech. Syst. Signal Proc. **208**, 110983 (2024).
9. Z. Li, J. Zhang, M. Wang, *et al.*, "An anti-noise ϕ-OTDR based distributed acoustic sensing system for high-speed railway intrusion detection," Laser Phys. **30**(8), 085103 (2020).
10. Z. Wang, L. Zhang, S. Wang, *et al.*, "Coherent Φ-OTDR based on I/Q demodulation and homodyne detection," Opt. Express **24**(2), 853–858 (2016).
11. X. Lu, M. A. Soto, P. J. Thomas, *et al.*, "Evaluating phase errors in phase-sensitive optical time-domain reflectometry based on I/Q demodulation," J. Lightwave Technol. **38**(15), 1 (2020).
12. C. Wang, Y. Shang, W. A. Zhao, *et al.*, "Distributed acoustic sensor using broadband weak FBG array for large temperature tolerance," IEEE Sens. J. **18**(7), 2796–2800 (2018).
13. C. Wang, C. Wang, Y. Shang, *et al.*, "Distributed acoustic map based on interferometry of phase optical time-domain reflectometry," Opt. Commun. **346**, 172–177 (2015).
14. P. Ma, Z. Sun, K. Liu, *et al.*, "Distributed fiber optic vibration sensing with wide dynamic range, high frequency response, and multi-points accurate location," Opt. Laser Technol. **124**, 105966 (2020).
15. A. Dandridge, A. B. Tveten, and T. G. Giallorenzi, "Homodyne demodulation scheme for fiber optic sensors using phase generated carrier," IEEE Trans. Microwave Theory Tech. **30**(10), 1635–1641 (1982).
16. H. Qian, B. Luo, H. He, *et al.*, "Phase demodulation based on DCM algorithm in φ-OTDR with self-interference balance detection," IEEE Photonics Technol. Lett. **32**(8), 473–476 (2020).
17. B. Liu, J. Lin, H. Liu, *et al.*, "Diaphragm-based long cavity Fabry–Perot fiber acoustic sensor using phase generated carrier," Opt. Commun. **382**, 514–518 (2017).
18. A. Zhang and S. Zhang, "High stability fiber-optics sensors with an improved PGC demodulation algorithm," IEEE Sens. J. **16**(21), 1 (2016).
19. A. N. Nikitenko, M. Y. Plotnikov, A. V. Volkov, *et al.*, "PGC-Atan demodulation scheme with the carrier phase delay compensation for fiber-optic interferometric sensors," IEEE Sens. J. **18**(5), 1985–1992 (2018).
20. S. Mu, B. Yu, L. Gui, *et al.*, "High-stability PGC demodulation technique with an additional sinusoidal modulation based on an auxiliary reference interferometer and EFA," Opt. Express **30**(15), 26941–26954 (2022).
21. S. Zhang, L. Yan, B. Chen, *et al.*, "Real-time phase delay compensation of PGC demodulation in sinusoidal phase-modulation interferometer for nanometer displacement measurement," Opt. Express **25**(1), 472–485 (2017).
22. J. Hu, W. Wang, B. Zhou, *et al.*, "Self-suppression of leading-fiber-induced noise for remote fiber-optic interferometric sensor using a dual-wavelength optical signal," Opt. Express **33**(4), 7533–7545 (2025).
23. Y. Tong, H. Zeng, L. Li, *et al.*, "Improved phase generated carrier demodulation algorithm for eliminating light intensity disturbance and phase modulation amplitude variation," Appl. Opt. **51**(29), 6962–6967 (2012).
24. S. Li, S. Shao, H. Mei, *et al.*, "Analysis and mitigation of the carrier phase delay effect of the digital phase generated carrier algorithm," Appl. Opt. **56**(3), 731–738 (2017).
25. A. Zhang and D. Li, "Interferometric sensor with a PGC-AD-DSM demodulation algorithm insensitive to phase modulation depth and light intensity disturbance," Appl. Opt. **57**(27), 7950–7955 (2018).
26. K. Sun, M. He, and L. Han, "Phase generated carrier demodulation method eliminating modulation depth influence," Acta Photonica Sinica **51**(6), 0606003 (2022).
27. W. Xiao, J. Cheng, D. Zhang, *et al.*, "An improved high stability and low distortion phase generated carrier demodulation algorithm for phase-sensitive optical time-domain reflectometers," Laser Phys. Lett. **19**(7), 075102 (2022).
28. G. Fang, T. Xu, S. Feng, *et al.*, "Phase-sensitive optical time domain reflectometer based on phase-generated carrier algorithm," J. Lightwave Technol. **33**(13), 2811–2816 (2015).
29. J. Park, W. Lee, and H. F. Taylor, "Fiber optic intrusion sensor with the configuration of an optical time-domain reflectometer using coherent interference of Rayleigh backscattering," Proc. SPIE **3555**, 49–56 (1998).
30. A. Masoudi and T. P. Newson, "High spatial resolution distributed optical fiber dynamic strain sensor with enhanced frequency and strain resolution," Opt. Lett. **42**(2), 290–293 (2017).
31. Y. Shang, Y. H. Yang, C. Wang, *et al.*, "Study on demodulated signal distribution and acoustic pressure phase sensitivity of a self-interfered distributed acoustic sensing system," Meas. Sci. Technol. **27**(6), 065201 (2016).